On the turbulence interface in magnetically confined plasmas

Tatsuya Kobayashi[1]

[1]*National Institute for Fusion Science, National Institutes of Natural Sciences, Toki 509-5292, Japan*

kobayashi.tatsuya@LHD.nifs.ac.jp

Abstract. In this contribution, two examples of the turbulence interface formation are shown. The first example is the turbulence interface at the edge transport barrier (ETB) in tokamak plasmas. Because of the radial electric field structure formation, the turbulence spatial structure is strongly modified. A model describing how the turbulence profile modification occurs is examined. The second example is the turbulence interface formed by a coexisting pair of instabilities observed in a linear magnetized plasma. Probe measurement reveals that the linearly driven drift wave excites a steep gradient of the parallel ion flow, which secondarily raises the parallel flow shear driven mode, the so-called D'Angelo mode. Although the habitats of these two modes are separated in radius, they oscillate simultaneously correlating with each other. Due to such dynamics, an interface of different modes self-consistently appears.

INTRODUCTION

A common feature of turbulence in magnetically confined plasmas, regardless of the confinement topology, is the formation of the self-sustained turbulence interface in a particular location. A representative example would be formation of the edge transport barrier (ETB) during the Low-confinement mode (L-mode) to High-confinement mode (H-mode) transition, being abbreviated as the L-H transition, in torus plasmas [1]. Because of its prospective capability for achieving a high performance plasma for the future nuclear reactor, the formation mechanism of the ETB has been intensively studied for the last two decades. The existence of the turbulence interface is a ubiquitous phenomenon in nature, and is seen in, e.g., a flow of neutral fluid [2], the solar tachocline [3], the atmospheric circulation [4]. The ultimate goal of that field from the view point of academic research would be to derive a prospective model that can describe the whole physics of the turbulence interface formation in various media. Before attacking this challenging problem, it is surely necessary to investigate each phenomenon in detail.

In this contribution, two examples of the turbulence interface formation are shown. The first example is the turbulence interface at the ETB in the JFT-2M tokamak. Because of the radial electric field structure formation, the turbulence spatial structure is strongly modified. A model describing how the turbulence profile modification occurs is examined. The second example is the turbulence interface formed by a coexisting pair of instabilities observed in a linear magnetized plasma PANTA. Probe measurement reveals that the linearly driven drift wave excites a steep gradient of the parallel ion flow, which secondarily raises the parallel flow shear driven mode, the so-called D'Angelo mode. Although the habitats of these two modes are separated in radius, they oscillate simultaneously correlating with each other. Due to such dynamics, an interface of different modes self-consistently appears.

TURBULENCE INTERFACE OBSERVED IN EDGE TRANSPORT BARRIER IN JFT-2M

After the first discovery of the H-mode [1], the physical mechanism responsible for the ETB formation has been intensely studied, and theoreticians predicted the importance of the radial electric field [5, 6]. Soon after the theoretical prediction was raised, experimentalists succeeded in observing the radial electric field structure at the peripheral region of the plasma as the theoreticians had predicted [7, 8]. Models focusing not only on the radial electric field formation mechanism [9] (see the review [10]) but also on turbulent transport suppression mechanism by the radial electric field [11, 12, 13] have been developed accordingly. Experimental validations are intensively promoted [14, 15, 16, 17, 18,

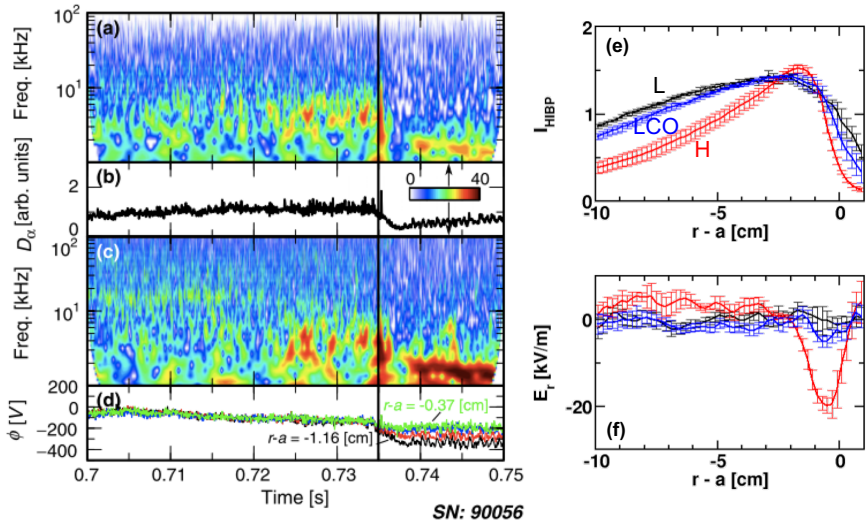

FIGURE 1. Typical time evolutions of (a) normalized wavelet power spectrum density and (b) raw signal of D_α emission intensity on the divertor. Time evolutions of (c) normalized wavelet power spectrum density and (d) raw signals of electrostatic potential evaluated at four HIBP sample volumes, where the signal at the most inner location is used to calculate (c) [23]. Mean radial profiles in (e) the HIBP intensity and (f) the radial electric field in the L-mode, H-mode and LCO periods [24].

19, 20, 21, 22]. However, these are still challenging mainly because of an insufficient precision of the turbulence and electric field measurements. In particular, the following open questions remain unsolved: (i) how is the radial electric field excited? (ii) how is the limit-cycle-oscillation (LCO), i.e., a sequential repetition of the L-H and H-L transitions, explained? and (iii) how is the turbulence transport quenched?

We attempt to solve these questions using a data set from JFT-2M. In some discharges, a heavy ion beam probe (HIBP) offered the direct measurement of the turbulence and the radial electric field with high spatial and temporal resolutions, which is one of the most ideal experimental data for the model validation.

Experimental setup and target plasma

JFT-2M is a medium size tokamak. Its major radius and minor radius are $R = 1.3$ m and $a = 0.3$ m, respectively. The target plasma is auxiliary heated by a codirected neutral beam injection (NBI) of the power of 750 kW. Other experimental conditions are: the line averaged electron density of 1.1×10^{19} m^{-3}, the toroidal magnetic field of ~ 1.2 T, the plasma current of 190 kA, and the safety factor at the flux surface enclosing 95 % of the total poloidal flux q_{95} of 2.9. The present experimental condition corresponds to the marginal operation on the L-H power threshold. An upper single-null divertor configuration is employed, where the ∇B drift is directed toward the X point. The plasma potential profile and fluctuation are measured by a heavy ion beam probe (HIBP). The upper boundary of the measurable frequency is $\sim$ 100 kHz, which is limited by an amplifier noise component. Four different spatial locations can be simultaneously measured, from which the fluctuation structure can be determined. The angle between the row of the sample volumes and the normal vector of the magnetic surface can be altered by changing the operating parameters of the HIBP. The peripheral region ($-5 < r - a < 0$ cm) of the top side of the torus is covered on a shot-to-shot basis.

Figures 1 (a)-(d) show the time evolution of the target discharge. Immidiately after the NB injection at $t = 0.7$ s, the geodesic acoustic mode (GAM) arises at $f \sim 15$ kHz in the potential fluctuation [25, 26]. Some hundreds millisecond later, the GAM is supplanted by the limit-cycle-oscillation (LCO) seen in the D_α and potential fluctuation spectra in $2 < f < 8$ kHz [23, 24, 27]. The L-H transition occurs at $t \sim 0.735$ s in this discharge (shown by the solid black line) [28, 29, 30, 31]. The radial profiles of the HIBP secondary beam intensity $I_{\rm HIBP}$ and the radial electric field are shown in Figs. 1 (e) and (f). Here, $I_{\rm HIBP}$ can be used as a proxy of the local electron density profile only at the very peripheral region, $r - a > -1.5$ cm, because the values at the core-side suffer the beam attenuation effect. Profiles in the L-mode and in the LCO periods are similar, except for a slightly stronger density gradient and a small E_r-well structure at the edge. After the H-mode transition, the edge density profile is characterized by the "pedestal"

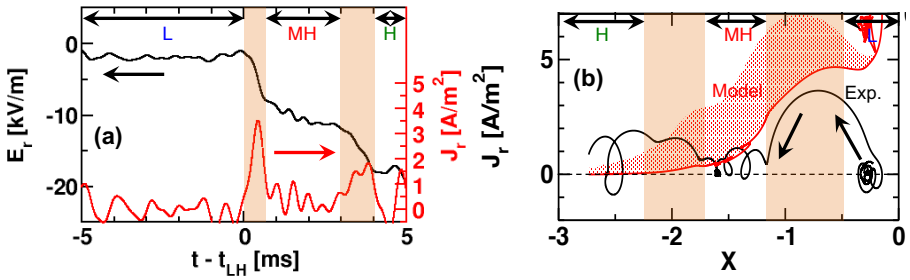

FIGURE 2. (a) Time evolutions of the radial electric field and the evaluated radial current. (b) The experimentally evaluated radial current and the radial current predicted by the sum of the loss-cone loss current and the neoclassical bulk viscosity current as a function of the normalized radial electric field [30].

structure realized by the ETB. The ETB is considered to be formed by the turbulence transport regulation by the E_r-well structure at $r - a \sim -0.7$ cm.

Physical mechanism of electric field excitation

Here, we consider the dynamics of the time derivative of the Poisson equation,

$$\epsilon_\perp \epsilon_0 \frac{\partial E_r}{\partial t} = -J_r, \tag{1}$$

where $\epsilon_\perp$ is the relative dielectric constant of toroidal plasmas [10] and is given as $\epsilon_\perp = 1 + M_{\rm tor} c^2/v_{\rm A}^2$, where $c/v_{\rm A}$ denotes the ratio between the speed of light and the Alfvén velocity $v_{\rm A} = B/\sqrt{n_{\rm i} m_{\rm i} \mu_0}$. Inertia enhancement factor $M_{\rm tor}$ in the banana regime is given as $M_{\rm tor} \sim 1 + 1.6 q^2/\sqrt{\epsilon_t}$, where q is the safety factor and $\epsilon_t = a/R$ is the inverse aspect ratio. The l.h.s. of Eq. (1) can be experimentally determined. The radial current, i.e., the r.h.s. of Eq. (1), can flow with various mechanisms. Some of them are theoretically modeled as

$$J_r = J_{\rm i}^{\rm lc} + J_{\rm i}^{\rm bv} - J_{\rm e-i}^{\rm wave} + J_{\rm i}^{v\nabla v} + J_{\rm i}^{\rm CX} + \text{others}. \tag{2}$$

The terms in the r.h.s refer to the loss-cone loss current, the neoclassical bulk viscosity current, the wave convection current, the Reynolds stress current, and the charge exchange damping [10]. The charge exchange contribution $J_{\rm i}^{\rm CX}$ is considered to be negligibly small in this discharge, because of the expected low edge neutral density due to the carbon wall and divertor [32]. The first four terms are explicitly given in Ref. [10] as a function of the plasma parameters. Nonlinearity of each current term with respect to the radial electric field can provides multiple states of the radial electric field [5, 6].

Figure 2 (a) shows the time evolution of the radial electric field and the experimentally estimated radial current at the E_r-well bottom. In JFT-2M, almost all L-H transition events are triggered by the sawtooth crash. From the time evolution, it is seen that the transition occurs twice. At the first transition, $t - t_{\rm LH} \sim 0$, where $t_{\rm LH}$ indicates the time in which the sawtooth heat pulse reaches the edge region, the radial electric field well is deepened down to $E_r \sim -10$ kV/m with the time scale of 100 μs. After a few milliseconds of a quasi-stationary state, the so-called meta-H-mode (MH-mode), the second transition occurs with a relatively slower time scale of 1 ms. The second transition is not triggered by the sawtooth crash. The well depth reaches $E_r \sim -20$ kV/m after the second transition. At the time instances of the two transition events, the radial current is induced. Since the time scale of the first transition is shorter than that of the second transition, the value of the positive radial current at the first transition is larger, $J_r \sim 3$ A/m^2.

The experimentally estimated J_r is compared to the theoretical models in Fig. 2 (b). Here, expected radial current of the sum of $J_{\rm i}^{\rm lc}$ and $J_{\rm i}^{\rm bv}$ is plotted as a function of the normalized radial electric field $X \equiv \rho_{\rm p} e E_r/T$, where $\rho_{\rm p}$ is the ion gyroradius at the poloidal magnetic field. When the plasma is in the L-mode, $X \sim 0$ and the experimentally evaluated radial current is zero. During the first transition, the positive radial current flows and the radial electric field is deepened down to $X \sim -1$. Then the radial current disappears. The second transition occurs at $X \sim -2$ with a relatively smaller radial current. Looking at the time period of the first transition, the theoretical model of $J_{\rm i}^{\rm lc} + J_{\rm i}^{\rm bv}$ well describes the experimental observation. However, there are two mismatches between the two curves. The first

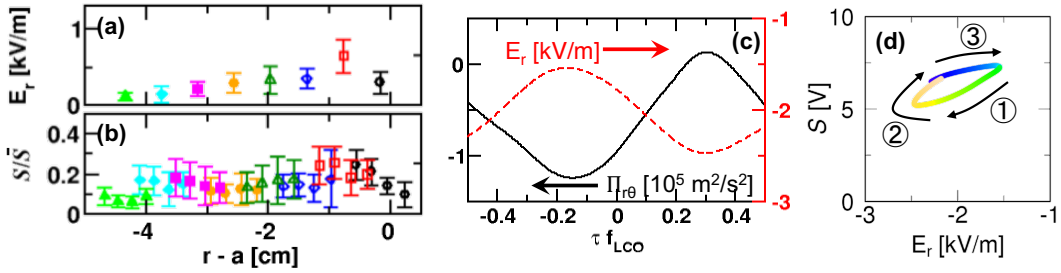

FIGURE 3. Radial profiles of LCO amplitude for (a) the radial electric field and (b) turbulence amplitude modulation. (c) Conditional averaged time evolutions of the Reynolds stress and the radial electric field [23]. (d) Lissajous diagram between the radial electric field and the turbulence amplitude modulation [24].

mismatch is at the second transition. The value of $J_{\rm i}^{\rm lc} + J_{\rm i}^{\rm bv}$ is strongly quenched by the large radial electric field so that the multiple transition cannot be explained by those models. The second mismatch is in the L-mode. Although the experimentally evaluated current is around zero, the model predicts a finite radial current, which is unreasonable. There should be other terms that make the total radial current to be zero.

From the direct turbulence measurement, the Reynolds stress term $J_{\rm i}^{v\nabla v}$ is considered to be one order of magnitude smaller than $J_{\rm i}^{\rm lc} + J_{\rm i}^{\rm bv}$ in the L-mode. Thus we concluded that this term plays a minor role both in the L-mode and during the transition. The fourth term, $J_{\rm e-i}^{\rm wave}$, could balance the excessive positive current. Using an intuitive model [5], it is expected that $J_{\rm e-i}^{\rm wave} < 0$ in this parameter regime and the magnitude of $J_{\rm e-i}^{\rm wave}$ can be comparable to $J_{\rm i}^{\rm lc} + J_{\rm i}^{\rm bv}$. Exploration of a more precise model of the wave convection contribution is demanded for more quantitative discussion for the L-mode current (momentum) balance problem.

Physical mechanism of limit-cycle oscillation

Approximately hundred milliseconds before the L-H transition, the LCO starts. A typical feature of the LCO is the quasi-periodic oscillation in D_α signal, i.e., the sequential repetition of the L-H and H-L transitions. Many other physical quantities, including the radial electric field, the electron density and its gradient, and the turbulence amplitude, are involved, as well. Figures 3 (a) and (b) show the radial profiles of the LCO amplitude in the radial electric field and the turbulence amplitude modulation, respectively. The LCO in E_r takes the maximal amplitude at $r - a \sim -0.8$, approximately the same location of the E_r-well bottom in the H-mode. The amplitude is $E_r \sim 500$ kV/m. At the location, the turbulence modulation amplitude also peaks with a relatively wider spatial structure. When the E_r structure is deepened by the LCO, the turbulence is suppressed and the density gradient increases so that the LCO is regarded to be the periodic generation/decay of a moderate transport barrier. In many other devices, including TJ-II [17] or DIII-D [18], it is claimed that the LCO can be explained by the "predator-prey model" between the zonal flow and turbulence [9]. We examine the idea in the case of JFT-2M.

If the predator-prey between the zonal flow and turbulence occurs, the Reynolds stress has to be sufficiently large to excite the zonal flow. Figure 3 (c) shows the conditional averaged time evolution of the Reynolds stress and the radial electric field as a function of the time normalized by the LCO frequency $f_{\rm LCO}$. The $E \times B$ velocity that is driven by the Reynolds stress can be evaluated as $|\Pi_{r\theta}| L^{-1} \epsilon_\perp^{-1} \omega_{\rm LCO}^{-1}$, where $|\Pi_{r\theta}|$ is the amplitude of the Reynolds stress modulation at the LCO frequency, L is the characteristic scale of the LCO, and $\omega_{\rm LCO} = 2\pi f_{\rm LCO}$ is the angular frequency of the LCO. The obtained value is the order of 10 m/s, where the experimentally evaluated $E \times B$ velocity modulation amplitude is $|E_r|/B \sim 500$ m/s. This analysis reveals that the Reynolds stress plays a minor role in driving the $E \times B$ velocity modulation.

By observing the phase difference between the electric field ($E \times B$ velocity) and the turbulence amplitude, one can discuss whether the predator-prey model explains the LCO. Figure 3 (d) shows the turbulence intensity S as a function of the radial electric field E_r at the location where the E_r modulation amplitude is maximum, $r - a \sim -0.8$ cm. The time sequence from the phase where $-E_r$ and S are maximum is as follows: (1) S decreases as $-E_r$ increases, possibly due to the turbulence suppression by E_r; (2) S increases while $-E_r$ remains approximately unchanged; and (3) $-E_r$ decreases while S remains approximately unchanged. This causal relation is opposite to the prediction of the

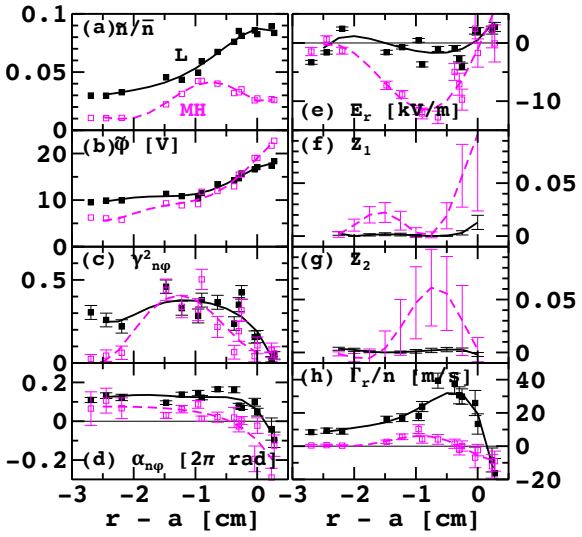

FIGURE 4. Radial profiles of (a) relative density fluctuation amplitude, (b) potential fluctuation amplitude, (c) and (d) squared cross coherence and cross phase between density fluctuation and potential fluctuation, respectively, (e) radial electric field, (f) shear parameter Z_1, (g) curvature parameter Z_2, and (h) particle flux normalized by mean density [31].

predator-prey model, because the prey (turbulence) should increase earlier than the predator (radial electric field) if the predator-prey model works. The present observation exemplifies the diversity of the LCO mechanism as discussed in Ref. [19]. A possible mechanism that explains the present LCO dynamics would be the E_r-bifurcation model [33], and its experimental validation remains for future investigations.

Physical mechanism of turbulence transport suppression

The problem regarding how the turbulence transport is reduced during the L-H transition is essential for predicting the turbulence transport level in the H-mode for ITER or future fusion devices. Historically, a model describing the turbulence amplitude reduction by the $E \times B$ shear [11] has been most frequently used, and numerous experimental validations have been performed [15, 16, 18]. After the publication of a pioneer work [14], in which importance of not only the $E \times B$ shear but also the curvature, and of not only the turbulence amplitude but also the phase difference between the potential fluctuation and the density fluctuation are suggested, a variety of routes to the reduced turbulence transport state in the H-mode are surveyed [21, 22]. In JFT-2M, the potential fluctuation and the density fluctuation below 100 kHz can be used for turbulence transport study. Here, we discuss the importance of both the E_r shear and curvature for the turbulence transport quench via both the amplitude suppression and the phase difference reduction.

By the theoretical model in Ref. [13], the shear factor Z_1 and the curvature factor Z_2 are quantified as

$$Z_1 \equiv \rho_{\rm i}^2 (V_{\rm d} B)^{-2} E_r'^2 \tag{3}$$

and

$$Z_2 \equiv -\rho_{\rm i}^2 (V_{\rm d} B)^{-2} (E_r - V_{\rm tor} B_\theta) E_r'', \tag{4}$$

respectively, where $\rho_{\rm i}$ is the ion gyro-radius, $V_{\rm d} \equiv T|n'|/enB$ is the diamagnetic velocity, and prime is the radial derivative. In the present case, the toroidal flow component in the radial electric field is considered to be much smaller, i.e., $E_r \gg V_{\rm tor} B_\theta$ [8], so that the toroidal velocity correction term for Z_2 is neglected. The amplitude of turbulence having a perpendicular wavenumber k is reduced as

$$I/I_0 = [1 + (k\rho_{\rm i})^{-2}(Z_1 + Z_2)]^{-1}, \tag{5}$$

where I and I_0 are the reduced turbulence amplitude and the intrinsic turbulence amplitude without E_r effects, respectively.

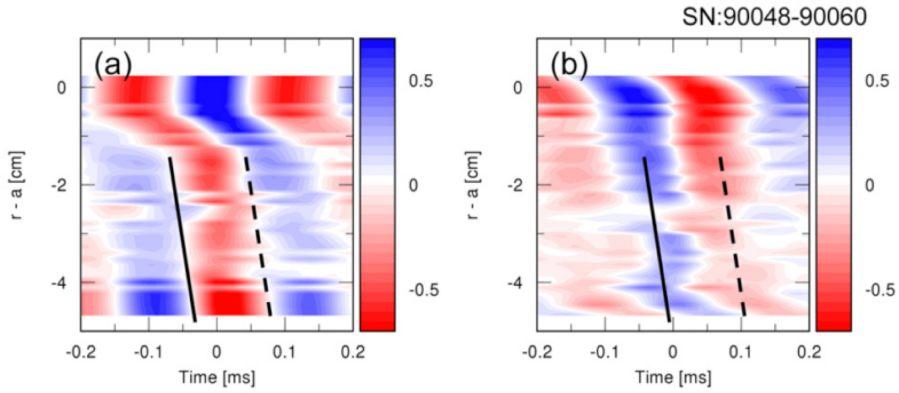

FIGURE 5. Cross correlation function of the LCO component of (a) the density fluctuation and (b) the turbulence amplitude modulation with respect to D_α [24].

Figure 4 shows the radial profiles of the turbulence properties as well as those of E_r, Z_1, and Z_2. The particle flux is defined as

$$\Gamma_r = B^{-1}(P_n P_\phi \gamma_{n\phi}^2)^{1/2} k_\theta \sin \alpha_{n\phi}, \tag{6}$$

where P_n and P_ϕ are the power spectrum of $\tilde{n}$ and $\tilde{\phi}$, and $\gamma_{n\phi}^2$ and $\alpha_{n\phi}$ are the squared cross coherence and cross phase between them, respectively [34]. After the L-MH transition, the particle transport shown in the panel (h) is strongly reduced. The particle flux is reduced mainly due to the density fluctuation amplitude suppression and the phase difference reduction. The density fluctuation amplitude reduction is larger where Z_1 is large and is limited in the E_r-well bottom, i.e., the location where $Z_1 \sim 0$ and Z_2 is large. The phase difference reduction occurs in the entire observable radius. However, at the outer shear region, the region where the negative phase difference exists, i.e., inward particle flux occurs, is widened. Even at the region where Z_2 is large and the density amplitude reduction is small, the particle flux is effectively suppressed by the phase difference reduction. This observation suggests that although the roles of Z_1 and Z_2 are different, both work for the turbulence transport reduction.

Transmission of turbulence clump

There is a long standing mystery regarding the confinement improvement during the ETB formation, that is, although the radial electric field structure formation occurs at the very edge region of the plasma, confinement is improved in a wide region from the core to the edge immidiately after the ETB formation [35]. This issue is sometimes referred to as the "nonlocality" of the turbulence transport. A clue for resolving the nonlocality during the ETB formation is found in the LCO dynamics. Figure 5 shows the cross correlation function of the density oscillation and the turbulence amplitude modulation at the LCO frequency, calculated with respect to the D_α signal. As shown in Fig. 3, the strong radial electric field is limited at the very edge region. However, the density front and the turbulence front propagate deeper in the inner radius. A mechanism of the turbulence front propagation, the so-called turbulence spreading theory, has been proposed [36]. The model predicts that the negative density gradient propagates prior to the turbulence clump. From the experimental data, the phase difference between them is approximately 0.2π, which is not in contradiction with the theory. The phase propagation velocity is estimated to be $\sim$ 900 m/s, which is of the order of the diamagnetic velocity. The propagation velocity is within the theoretical prediction as well. A similar turbulence clump propagation enhanced by the GAM is theoretically predicted [37] and experimentally observed [38]. Quantification of the impact of the turbulence clump propagation on the plasma confinement is an interesting and important issue for future study.

TURBULENCE INTERFACE OBSERVED IN LINEAR MAGNETIZED PLASMA PANTA

One of the largest advantages in basic linear devices is that one can routinely use Langmuir probes. By utilizing a Mach probe array designed for measurement of the axial flow, the axial momentum transport and the particle transport, a

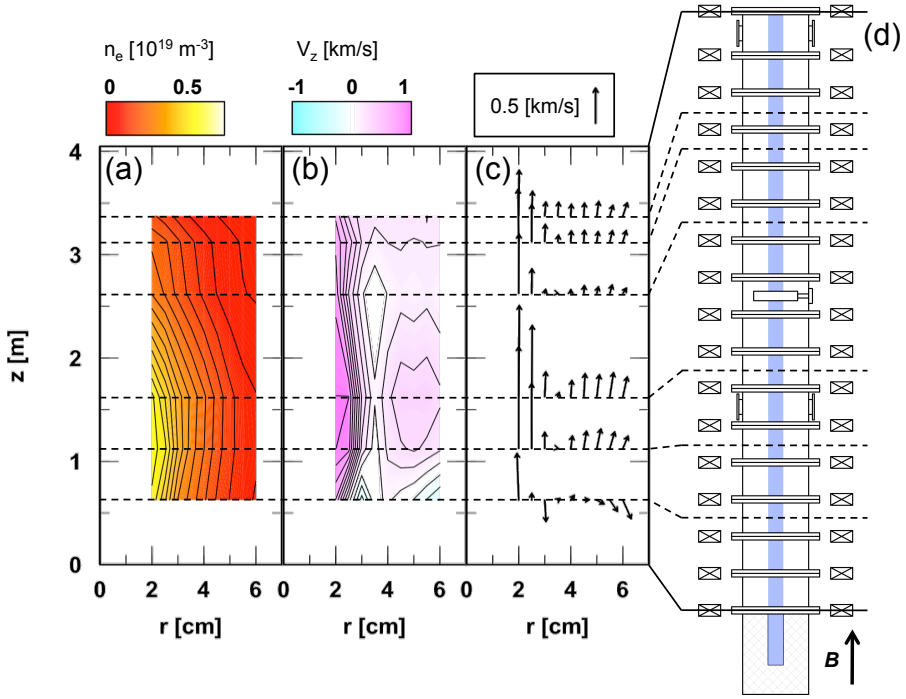

FIGURE 6. Mean profiles (a) of the electron density, (b) of the axial ion velocity, and (c) of the velocity vector, and (d) schematic view of the PANTA device. Dashed horizontal lines show the measurement axial locations [39].

new paradigm of the study, i.e., mutual interaction between the density gradient driven drift wave and the parallel flow shear driven D'Angelo mode, is opened. In this contribution, a spontaneous interface formation between the two modes and their curious coexistence is shown.

Experimental set up and target plasma

The experiments are performed in the Plasma Assembly for Nonlinear Turbulence Analysis (PANTA). The dimensions of the plasma column are: the axial length of ~ 4 m and the plasma radius of ~ 5 cm. The plasma is produced by the helicon discharge with the rf power of 3 kW at one side of the column. The other side of the column is terminated by the stainless end-plate, around which the plasma is subject to the recombination process. The homogeneous axial magnetic field of 90 mT confines the plasma radially, and the plasma freely flows axially. In PANTA, the neutral gas pressure is an important control parameter, and by changing the neutral gas pressure nonlinearity of plasma oscillation varies [40]. In this experiment, the neutral gas pressure is set to be 0.1 Pa, at which the so-called streamer structure is observed. Here, the origin of the axial coordinate (z) is defined as the edge of the plasma column at the source region side, as shown in Fig. 6 (d). The azimuthal direction (θ) is defined as the electron diamagnetic direction. The electron density, the azimuthal electric field, and the axial flow velocity are measured with the Mach probe array in the radius (r)-axial direction (z) dimension.

Figure 6 (a) shows the electron density profile. The electron density profile peaks in the core region, and has a gradient in the axial direction, as well. From numerical study, it is predicted that the density gradient driven resistive drift wave is unstable in this operation regime. Figures 6 (b) and (c) show the axial flow velocity profile and the vector field of the axial flow and the radial flow. Here, the axial flow is measured by the Mach probe. In principle, the value measured here includes both the flow velocity contribution and the diffusion flux contribution, while our interest is only the former. Although a long mean free path and a high collision frequency make a relatively large diffusion

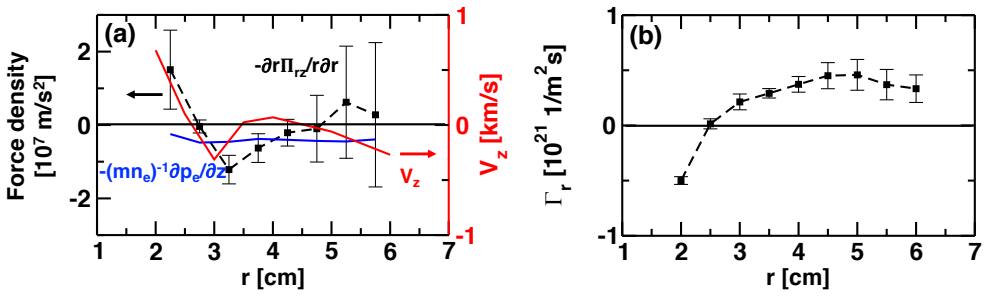

FIGURE 7. Radial profiles (a) of the axial Reynolds force density and the axial flow velocity and (b) of the turbulent particle flux [39].

coefficient along the magnetic field of $D \sim O(10^3)$ m^2/s, the density gradient is almost zero in the half of the plasma column at the source region side, $z < 2$ m [see Fig. 6 (a)]. Therefore, the diffusion flux contribution is negligibly small in that part. The discussion below is thus valid in that location. The stationary radial flow is considered to be negligibly small since particles are radially confined by the axial magnetic field. Even with the radial confinement, a finite net radial flow can be driven by the diffusion process or turbulent transport process given by Eq. (6). In the present case the latter dominates over the former, therefore the radial flow velocity is defined as Γ_r/n_e. A strong axial flow from the source region to the end-plate region is observed at the core region ($r < 2.5$ cm). At $2.5 < r < 3.5$ cm, the strong axial flow shear region is driven, which may be due to axial momentum transport by the plasma turbulence. Further outside, the flow increases again. The flow inversion occurs at $z = 0.625$ m and $r = 3$ cm. To study how these complicated flow structures are driven, the axial momentum flux and the particle flux driven by the turbulence are analyzed.

Axial momentum flux and particle flux

Axial Reynolds stress is defined as

$$\Pi_{rz} = \langle \tilde{V}_z \tilde{V}_r \rangle + \bar{V}_z \langle \tilde{V}_r \tilde{n}_e/\bar{n}_e \rangle + \langle \tilde{V}_z \tilde{V}_r \tilde{n}_e/\bar{n}_e \rangle, \tag{7}$$

where the radial velocity fluctuation is defined as the $E \times B$ velocity $\tilde{V}_r = \tilde{E}_\theta/B$. To examine how the observed axial flow profile is driven, the two-fluid equation of motion for electrons and ions are coupled. It is given as:

$$0 = -V_z \frac{\partial V_z}{\partial z} - V_r \frac{\partial V_z}{\partial r} - (m_i n_i)^{-1} \frac{\partial p}{\partial z} - \frac{\partial r\Pi}{r\partial r} - \nu_{in} V_z, \tag{8}$$

where p is the total pressure $p_e + p_i$, i.e., the sum of the electron pressure and the ion pressure, m_i is the ion mass, and $\nu_{in} \sim 40$ kHz is the ion-neutral collision frequency. The ion density n_i is considered to be equal to the electron density n_e due to the quasi-neutrality. Here, the ion cyclotron frequency is comparable to ν_{in} so that estimation of plasma dynamics using $E \times B$ may not be completely valid. Nevertheless, the above model seems to capture the feature of the flow formation as discussed below. For more quantitative discussion, a dedicated model must be developed for the partially magnetized plasmas. Terms in the r.h.s. are called the inertia terms from the axial and radial derivatives, the pressure term, the parallel Reynolds stress term, and the neutral drag term. The first four terms correspond to the flow excitation force, and the last term is the drag force that balances the excitation force. In this experiment, the inertia terms are confirmed to be negligibly small.

Figure 7 (a) shows the pressure term and the Reynolds stress term in Eq. 8, as well as the axial flow profile at $z = 0.625$ m. Considering the value of ν_{in}, the Reynolds force density and $\nu_{in} V_z$ are approximately in the same order of magnitude. As can be seen, the Reynolds stress force profile and the axial flow profile are in reasonable agreement. Therefore, the axial flow reversal can be explained by the turbulent momentum transport. Due to the redistribution of the axial flow profile, a strong shear region emerges at $r < 2.5$ cm. The pressure term plays a minor role.

Figure 7 (b) shows the radial profile of the turbulent particle flux. The polarity changes from negative to positive at $r = 2.5$ cm, implying that the resistive drift wave is only unstable in $r > 2.5$ cm. Linear stability analysis [41] revealed that the axial flow shear driven mode, the so-called D'Angelo mode, can be unstable at $r < 2.5$ cm. The

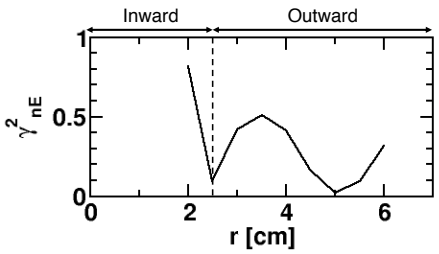

FIGURE 8. Radial profile of squared cross coherence between the azimuthal electric field fluctuation at $(z, r) = (0.625\ \mathrm{m}, r)$ and the density fluctuation at $(z, r) = (2.125\ \mathrm{m}, 40\ \mathrm{mm})$ [39].

energy source of the D'Angelo mode is maintained by the resistive drift wave. Then, a question arises: How do these two modes interact with each other?

Figure 8 shows the relative cross correlation between a reference probe at (z, r)=(2.125 m, 4 cm), where the resistive drift wave is dominant. Surprisingly, the spatial correlation between the resistive drift wave and the D'Angelo mode is quite high, ~ 0.8. The two modes oscillate together, keeping a phase relation. These types of strong correlations between different kinds of instabilities involving transport and structure formation are defined as the concept of the "cross-ferroic turbulence" [42]. Due to such dynamics, an interface of different modes self-consistently appears.

SUMMARY

In this contribution, two examples of the turbulence interface formation were shown. The first example was the turbulence interface at the ETB in the JFT-2M tokamak. Because of the radial electric field structure formation, the turbulence spatial structure was strongly modified. A model describing how the turbulence profile modification occurs was examined. The second example was the turbulence interface formed by a coexisting pair of instabilities observed in a linear magnetized plasma PANTA. Probe measurement revealed that the linearly driven drift wave excites a steep gradient of the parallel ion flow, which secondarily raises the parallel flow shear driven mode, the so-called D'Angelo mode. Although the habitats of these two modes were separated in radius, they oscillate simultaneously correlating with each other. Due to such dynamics, an interface of different modes self-consistently appeared.

ACKNOWLEDGMENTS

This article is dedicated to Prof. K. Itoh and Prof. S.-I. Itoh on the occasion of their retirements. The author also appreciates Drs. K. Ida, T. Ido, A. Fujisawa, S. Inagaki, Y. Nagashima, T. Yamada, N. Kasuya, M. Sasaki, Y. Kosuga, H. Arakawa, K. Kamiya, K. Hoshino, and Y. Miura for useful discussions and the late Dr. H. Maeda and Drs. Y. Hamada, M. Mori, Y. Kamada and S. Sakakibara for strong support. This work is partly supported by JSPS KAKENHI Grant Numbers 21224014, 23244113, 15H02155, and 16H02442, by collaboration programs with QST and with the RIAM of Kyushu University, and by the Asada Science Foundation.

REFERENCES

[1] F. Wagner *et al.*, Phys. Rev. Lett. **49**, 1408–1412 (1982).
[2] D. Barkley, B. Song, V. Mukund, G. Lemoult, M. Avila, and B. Hof, Nature **526**, p. 550 (2015).
[3] D. W. Hughes, R. Rosner, and N. O. Weiss, *The Solar Tachocline* (Cambridge University Press, 2007).
[4] J. G. Charney, Geophys. Publ. **17**, p. 1 (1948).
[5] S.-I. Itoh and K. Itoh, Phys. Rev. Lett. **60**, 2276–2279 (1988).
[6] K. C. Shaing and E. C. Crume Jr, Phys. Rev. Lett. **63**, p. 2369 (1989).
[7] R. J. Groebner, K. H. Burrell, and R. P. Seraydarian, Phys. Rev. Lett. **64**, p. 3015 (1990).
[8] K. Ida *et al.*, Phys. Rev. Lett. **65**, 1364–1367 (1990).
[9] E. J. Kim and P. H. Diamond, Phys. Rev. Lett. **90**, p. 185006 (2003).
[10] K. Itoh and S.-I. Itoh, Plasma Phys. Control. Fusion **38**, p. 1 (1996).

[11] H. Biglari, P. H. Diamond, and P. W. Terry, Phys. Fluids B **2**, p. 1 (1990).
[12] S.-I. Itoh and K. Itoh, J. Phys. Soc. Jpn. **59**, p. 3815 (1990).
[13] K. Itoh *et al.*, Nucl. Fusion **57**, p. 022005 (2017).
[14] R. A. Moyer *et al.*, Phys. Plasmas **2**, 2397–2407 (1995).
[15] K. H. Burrell, Phys. Plasmas **4**, p. 1499 (1997).
[16] G. D. Conway *et al.*, Phys. Rev. Lett. **106**, p. 65001 (2011).
[17] T. Estrada *et al.*, Europhys. Lett. **92**, p. 35001 (2010).
[18] L. Schmitz *et al.*, Phys. Rev. Lett. **108**, p. 155002 (2012).
[19] J. Cheng, J. Dong, K. Itoh, L. Yan, M. Xu, K. Zhao, W. Hong, Z. Huang, X. Ji, W. Zhong, *et al.*, Phys. Rev. Lett. **110**, p. 265002 (2013).
[20] I. Shesterikov, Y. Xu, *et al.*, Phys. Rev. Lett. **111**, p. 055006 (2013).
[21] J. A. Boedo *et al.*, Nucl. Fusion **42**, p. 117 (2002).
[22] K. Kamiya, K. Itoh, and S.-I. Itoh, Sci. Rep. **6**, p. 30585 (2016).
[23] T. Kobayashi, K. Itoh, T. Ido, K. Kamiya, S.-I. Itoh, Y. Miura, Y. Nagashima, A. Fujisawa, S. Inagaki, K. Ida, *et al.*, Phys. Rev. Lett. **111**, p. 035002 (2013).
[24] T. Kobayashi, K. Itoh, T. Ido, K. Kamiya, S.-I. Itoh, Y. Miura, Y. Nagashima, A. Fujisawa, S. Inagaki, K. Ida, *et al.*, Nucl. Fusion **54**, p. 073017 (2014).
[25] T. Ido, Y. Miura, K. Kamiya, Y. Hamada, K. Hoshino, A. Fujisawa, K. Itoh, S. Itoh, A. Nishizawa, H. Ogawa, *et al.*, Plasma Phys. Control. Fusion **48**, p. S41 (2006).
[26] T. Kobayashi, M. Sasaki, T. Ido, K. Kamiya, Y. Miura, Y. Nagashima, K. Ida, S. Inagaki, A. Fujisawa, S.-I. Itoh, *et al.*, Phys. Rev. Lett. **120**, p. 045002 (2018).
[27] K. Itoh, S.-I. Itoh, and A. Fujisawa, Plasma Fusion Res. **8**, p. 1102168 (2013).
[28] T. Kobayashi, K. Itoh, T. Ido, K. Kamiya, S.-I. Itoh, Y. Miura, Y. Nagashima, A. Fujisawa, S. Inagaki, K. Ida, *et al.*, Nucl. Fusion **55**, p. 063009 (2015).
[29] T. Kobayashi, K. Itoh, T. Ido, K. Kamiya, S.-I. Itoh, Y. Miura, Y. Nagashima, A. Fujisawa, S. Inagaki, K. Ida, *et al.*, Sci. Rep. **6**, p. 30720 (2016).
[30] T. Kobayashi, K. Itoh, T. Ido, K. Kamiya, S.-I. Itoh, Y. Miura, Y. Nagashima, A. Fujisawa, S. Inagaki, K. Ida, *et al.*, Nucl. Fusion **57**, p. 072005 (2017).
[31] T. Kobayashi, K. Itoh, T. Ido, K. Kamiya, S.-I. Itoh, Y. Miura, Y. Nagashima, A. Fujisawa, S. Inagaki, and K. Ida, Sci. Rep. **7**, p. 14971 (2017).
[32] K. Itoh and S.-I. Itoh, Plasma Phys. Control. Fusion **37**, p. 491 (1995).
[33] S.-I. Itoh, K. Itoh, A. Fukuyama, and Y. Miura, Phys. Rev. Lett. **67**, 2485–2488 (1991).
[34] E. J. Powers, Nucl. Fusion **14**, p. 749 (1974).
[35] J. G. Cordey, D. G. Muir, S. V. Neudachin, V. V. Parail, E. Springmann, and A. Taroni, Nucl. Fusion **35**, p. 101 (1995).
[36] T. S. Hahm, P. H. Diamond, Z. Lin, K. Itoh, and S.-I. Itoh, Plasma Phys. Control. Fusion **46**, p. A323 (2004).
[37] M. Sasaki, T. Kobayashi, K. Itoh, N. Kasuya, Y. Kosuga, A. Fujisawa, and S.-I. Itoh, Phys. Plasmas **25**, p. 012316 (2018).
[38] T. Kobayashi, M. Sasaki, K. Itoh, T. Ido, K. Kamiya, S.-I. Itoh, Y. Miura, Y. Nagashima, A. Fujisawa, S. Inagaki, and K. Ida, "Interaction of geodesic acoustic modes and turbulence in JFT-2M tokamak," in *16th International Workshop on H-mode Physics and Transport Barriers* (St. Petersburg, 2017) p. A4.
[39] T. Kobayashi, S. Inagaki, Y. Kosuga, M. Sasaki, Y. Nagashima, T. Yamada, H. Arakawa, N. Kasuya, A. Fujisawa, S.-I. Itoh, *et al.*, Phys. Plasmas **23**, p. 102311 (2016).
[40] T. Kobayashi, S. Inagaki, M. Sasaki, Y. Kosuga, H. Arakawa, F. Kin, T. Yamada, Y. Nagashima, N. Kasuya, A. Fujisawa, *et al.*, Plasma Fusion Res. **12**, 1401019–1401019 (2017).
[41] Y. Kosuga, S.-I. Itoh, and K. Itoh, Plasma Fusion Res. **10**, p. 3401024 (2015).
[42] S. Inagaki, T. Kobayashi, Y. Kosuga, S.-I. Itoh, T. Mitsuzono, Y. Nagashima, H. Arakawa, T. Yamada, Y. Miwa, N. Kasuya, *et al.*, Sci. Rep. **6**, p. 22189 (2016).